NeuroImage 236 (2021) 118078

Contents lists available at ScienceDirect

NeuroImage

journal homepage: www.elsevier.com/locate/neuroimage

Strain Tensor Imaging: Cardiac-induced brain tissue deformation in humans quantified with high-field MRI

Jacob Jan Sloots[a,*], Geert Jan Biessels[b], Alberto de Luca[b], Jaco J.M. Zwanenburg[a]

[a] Radiology, University Medical Center Utrecht, the Netherlands
[b] Neurology, UMC Utrecht Brain Center, University Medical Center Utrecht, the Netherlands

ARTICLE INFO

Keywords:
Brain Deformation
Strain Tensor
Tissue Strain
Single-Shot DENSE
Poisson effect
Microvasculature
Magnetic Resonance Imaging
Small Vessel Disease

ABSTRACT

The cardiac cycle induces blood volume pulsations in the cerebral microvasculature that cause subtle deformation of the surrounding tissue. These tissue deformations are highly relevant as a potential source of information on the brain's microvasculature as well as of tissue condition. Besides, cyclic brain tissue deformations may be a driving force in clearance of brain waste products. We have developed a high-field magnetic resonance imaging (MRI) technique to capture these tissue deformations with full brain coverage and sufficient signal-to-noise to derive the cardiac-induced strain tensor on a voxel by voxel basis, that could not be assessed non-invasively before. We acquired the strain tensor with 3 mm isotropic resolution in 9 subjects with repeated measurements for 8 subjects. The strain tensor yielded both positive and negative eigenvalues (principle strains), reflecting the Poison effect in tissue. The principle strain associated with expansion followed the known funnel shaped brain motion pattern pointing towards the foramen magnum. Furthermore, we evaluate two scalar quantities from the strain tensor: the volumetric strain and octahedral shear strain. These quantities showed consistent patterns between subjects, and yielded repeatable results: the peak systolic volumetric strain (relative to end-diastolic strain) was $4.19{\cdot}10^{-4} \pm 0.78{\cdot}10^{-4}$ and $3.98{\cdot}10^{-4} \pm 0.44{\cdot}10^{-4}$ (mean ± standard deviation for first and second measurement, respectively), and the peak octahedral shear strain was $2.16{\cdot}10^{-3} \pm 0.31{\cdot}10^{-3}$ and $2.31{\cdot}10^{-3} \pm 0.38{\cdot}10^{-3}$, for the first and second measurement, respectively. The volumetric strain was typically highest in the cortex and lowest in the periventricular white matter, while anisotropy was highest in the subcortical white matter and basal ganglia. This technique thus reveals new, regional information on the brain's cardiac-induced deformation characteristics, and has the potential to advance our understanding of the role of microvascular pulsations in health and disease.

1. Introduction

Blood flow into the brain is pulsatile, driven by variation in blood pressure over the cardiac cycle. The pulsatile pressure waves, generated by the heart, are transmitted through the arterial tree all the way to the level of the microvasculature (Hahn et al., 1996, Shore et al., 1995) As the arterial pressure wave reaches the microvascular bed, these microvessels swell and stretch elastically causing the surrounding tissue to be displaced (Reese et al., 2002, Soellinger et al., 2009, Zhong et al., 2009). These ensuing subtle tissue deformations show regional variation, depending on the amount of blood that is delivered locally, but also on tissue properties and the tissue's position relative to, for example, the ventricles.

Measuring brain pulsatility is of interest, as it carries information of both the blood vessels that drive these pulsations, and of the surrounding tissue that deforms in response to the vascular pulse. Indeed, it has been shown that brain tissue stiffness can be derived by performing magnetic resonance elastography (MRE) reconstructions on measured heartbeat-related tissue motions (Weaver et al., 2012, Zorgani et al., 2015). Conventional MRE has shown that the brain tissue softens (becomes less stiff) with age, which probably reflects change in the tissues microstructure (Sack et al., 2009). Also, one can compute the volumetric strain accompanying the brain tissue displacement, which is defined as the relative change in volume of an elementary piece of tissue (Hirsch et al., 2013, Adams et al., 2020, Sloots et al., 2020, Adams et al., 2019). Regional variation in this volumetric strain most likely reflects (at least partially) regional variation in the arterial blood fraction of the tissue (Adams et al., 2019). This notion is corroborated by observed white matter tissue swelling during systole, which is much smaller than the gray matter tissue swelling (Adams et al., 2020, Sloots et al., 2020, Adams et al., 2019). It is conceivable that combining dedicated computer models with precise measurements of the brain tissue deformation would yield insight in mechanical properties of both the vasculature (such as local blood volume and its compliance) and the tissue (such as the bulk- and shear modulus) (Linninger et al., 2005, Linninger et al., 2009)

* Corresponding author.
E-mail address: j.j.sloots@umcutrecht.nl (J.J. Sloots).

https://doi.org/10.1016/j.neuroimage.2021.118078.
Received 8 December 2020; Received in revised form 2 February 2021; Accepted 7 April 2021
Available online 18 April 2021.

Apart from offering a window to microvascular and tissue microstructural features, brain tissue pulsations are also of interest for their potential role in essential physiological processes. Flow-induced shear stress and its pulsatility evoke mechanotransductive responses in endothelial cells, which constitute the blood-brain barrier (Davies et al., 2013, Chistiakov et al., 2017, Dai et al., 2004). Moreover, tissue deformations propel cerebral spinal fluid (CSF) around the brain. As CSF fulfills an important role in the drainage of cerebral waste, tissue deformation is considered to contribute to waste clearance in the brain (Mestre et al., 2017, Spector et al., 2015). Although the exact mechanism of brain waste clearance are still controversial, it is likely that tissue deformations contribute this process by mixing of the interstitial and para-arterial fluids (Asgari et al., 2016, Bakker et al., 2016). Non-invasive assessment of brain tissue pulsations may therefore be of value for studying brain physiology, and could also be relevant for brain disease. For instance, stiffening of the vascular walls is known to be associated with increased risk of stroke and the development of cerebral small vessel disease (cSVD). cSVD is a major cause of stroke and dementia that can currently only be detected when macroscopic, mostly irreversible, tissue lesions have been developed (Wardlaw et al., 2013, Pantoni, 2010). Assessment of changes in the microvascular- and tissue properties prior to the development of such damage might yield insight in the underlying disease processes.

Despite the apparent relevance of cardiac-induced brain tissue deformations, there are currently limited methods to study these deformations in a non-invasive way in humans. The phenomenon of physiological brain tissue deformation is subtle, with typically maximal stretch along a single direction in the order of 0.3% (Sloots et al., 2020, Pahlavian et al., 2018). Volumetric strains are even more subtle, typically less than approx. 0.1% (Adams et al., 2020, Sloots et al., 2020, Adams et al., 2019). These deformations can be derived from motion field maps through the use of spatial derivatives. MRI techniques that in principle can provide these motion field maps include amplified MRI (aMRI) (Holdsworth et al., 2016, Terem et al., 2018) and phase-contrast MRI (PC-MRI) (Ståhlberg et al., 1989, Feinberg and Mark, 1987). Yet, aMRI is designed for standard anatomical cine images, which are not optimized to capture the subtle brain motion. Besides, the aMRI algorithms do not provide deformation fields directly, meaning that additional registration algorithms have to be used that only add to uncertainty. On the other hand, PC-MRI requires velocity sensitivities (V_{encs}) in the order of 1 mm/s, which require bipolar gradients that are too large to be practically feasible with reasonable TRs and TEs (practically feasible V_{encs} are in the order of 1 cm/s) (Adams et al., 2020). Therefore, we use Displacement Encoding with Stimulated Echoes (DENSE) (Aletras et al., 1999) to quantify these motion field maps (Reese et al., 2002, Soellinger et al., 2009, Zhong et al., 2009). However, the computation of spatial derivatives amplifies the noise present in these motion field maps. As a result, the signal to noise ratio (SNR) in the strain measurements are typically low. Even at 7T, current strain measurements as obtained with a time-resolved multi-shot 3D approach, require an increase in SNR by approximately a factor of 10, in order to perform a voxel-wise analysis of the tissues volumetric strain (Adams et al., 2019). The lack in SNR in the multi-shot 3D approach mainly originated from the use of sub-optimal encoding sensitivities of the DENSE sequence. In these studies, less-than optimal motion encoding sensitivity already induced considerably ghosting artifacts due to phase inconsistencies between the shots, which were due to involuntary subject motion resulting from, among other things, respiration (Soellinger et al., 2009, Adams et al., 2019). This sensitivity to involuntary motion prohibited the use of the theoretically optimal motion encoding sensitivity. The recently proposed DENSE sequence (Sloots et al., 2020) circumvents these phase inconsistencies by using a single-shot approach, thereby enabling to increase the motion sensitivity that yields higher SNR in the motion field maps (Sloots et al., 2019). Moreover, as this approach is less sensitive to subject motion it may be more advantageous to use in patients. Yet, this technique was limited in brain coverage by the 2D acquisitions.

In this work, we present a comprehensive single-shot DENSE sequence with optimized sensitivity that combines the benefit of high SNR for a voxel-wise strain analysis, and a simultaneous multi-slice (SMS) acquisition approach for whole-brain coverage. We use the technique to derive the cardiac-induced tissue deformations and characterize this deformation across the brain. Specifically, we derive the full strain tensor and map it for the entire brain. Besides, we present two scalar maps derived from the tensor: volumetric strain and octahedral shear strain. First, a brief background on the derivation of the strain tensor is provided, which summarizes the established relevant theory. The heart of this work, however, is the acquisition of deformation gradient fields with sufficient SNR that make the strain tensor reconstruction feasible, without suffering from excessive noise. We acquire the strain tensor in multiple subjects to investigate its inter-subject consistency and also include repeated measurements to assess its repeatability. By combining the data from 9 subjects to MNI space, we aim to quantitatively describe the typical pattern of cardiac-induced brain tissue deformation.

2. Materials and methods

2.1. DENSE sequence

The DENSE sequence (Aletras et al., 1999) consists of a motion encoding and decoding part (see Fig. 1). The encoding part consists of a gradient between two 90° RF pulses, which imposes a sinusoid on the longitudinal magnetization of which the local phase encodes the current position of the tissue. After a given time, the decoding part reads out the prepared longitudinal magnetization. Any tissue displacement along the direction of the encoding gradient leads to a corresponding phase shift in the resulting phase image. This way, DENSE – analogue to velocity encoding – manipulates the phase information such that it becomes proportional to the displacement of brain tissue that occurred between encoding and decoding.

Tissue displacement maps (u_x, u_y, u_z) can be derived from motion-sensitive phase images acquired through DENSE by

$$u_x = \frac{D_{enc}}{\pi}\phi_x \tag{1}$$

where ϕ_x is the phase of the DENSE MRI signal acquired after motion encoding in the x-direction and D_{enc} is the displacement encoding value in units of meters (similar to the V_{enc} parameter used in phase-contrast MRI, which has units of meters/second). At this point, the MRI phase signal contains both phase contributions due to cardiac-induced motion, subject motion and phase confounders from respiration and the RF coils, which are later regressed out after computing the deformation gradients.

2.2. Simultaneous multi-slice dense

Our previous developed cardiac triggered, single-shot DENSE sequence (Sloots et al., 2020) was modified to be compatible with a simultaneous multi-slice (SMS) acquisition approach to obtain time- and SNR-efficient whole brain DENSE acquisitions (Barth et al., 2016). While the encoding part of the DENSE sequence (first two RF pulses) remained unchanged and non-selective, the third RF pulse for slice selective excitation needed modification to be compatible with a multiband SENSE acquisition approach (Barth et al., 2016). We achieved this by replacing the standard excitation pulse with a SMS excitation pulse as implemented by the vendor on the scanner for other sequences. This SMS excitation pulse combines a standard two-lobe sinc pulse with two frequency offsets to obtain a user defined spacing (72 mm in our case) between the slices. The duration of the multiband RF pulses was longer compared to the standard RF-pulse (3.39 ms vs 1.13 ms). The simultaneously acquired volumes were reconstructed by the standard reconstruction platform of the scanner. A full evaluation of the SMS method for the proposed DENSE sequence is provided in the supplementary file (Figures S1 and S2).

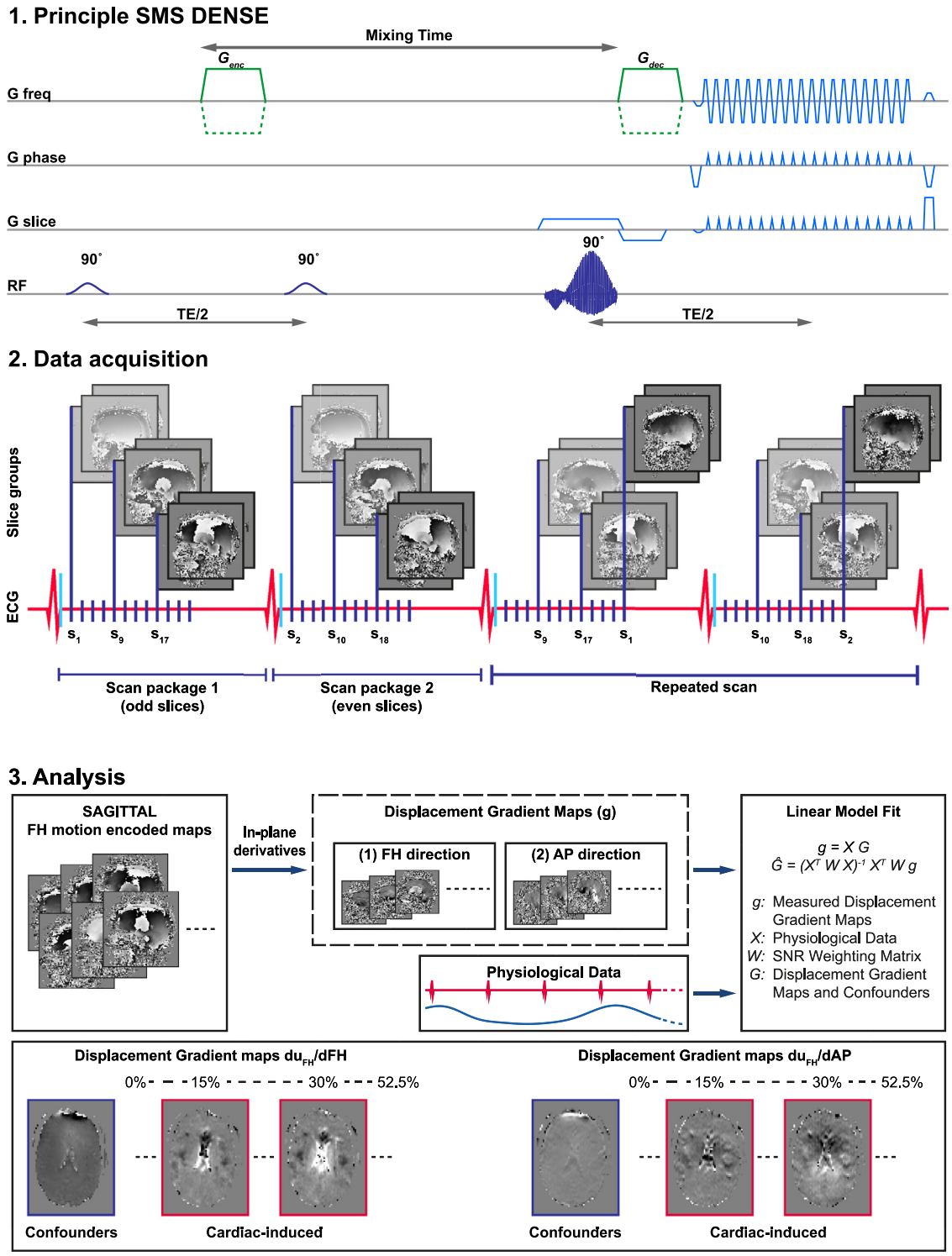

Fig. 1. Simultaneous multi-slice (SMS) DENSE acquisition principle, combined with an example for data acquisition and analysis of one DENSE series. In the current example, motion encoding was in the Feet-to-Head direction with a sagittal acquisition orientation. Repeating the DENSE MRI sequence for additional in-plane encoding directions with sagittal, coronal and transverse orientation, resulted in 6 datasets.

(1) SMS DENSE consists of 2 non-selective 90˚ RF pulses to encode the tissue. After a given mixing-time, a selective 90˚ multi-band RF pulse is employed to excite and acquire (in the current method) a slice group of 3 2D slices.

(2) Data was recorded over 24 repeated acquisitions with alternating encoding direction sign to distinguish between phase contributions due to motion and a motion independent phase confounders. Each repeated acquisition consisted of 12 excitations in each package with a multi-band factor of 3, which equals to 72 slices. Odd slices (associated with excitations s_1, s_3 … s_{23}) were acquired in the first package whereas the even slices (associated with excitations s_2, s_4 … s_{24}) were acquired in the second package. Slice order was permuted over the repeated acquisitions to obtain each slice at different moments in the cardiac cycle.

(3) Time-series of displacement-encoded phase images (d) were used to derive displacement gradient maps (g, two maps for each encoding direction). The current sagittal example yields the $\frac{\partial u_{FH}}{\partial FH}$ and $\frac{\partial u_{FH}}{\partial AP}$ displacement gradients, which are shown here in transverse orientation to illustrate the full brain coverage with isotropic voxels. Using the physiological data, these gradient maps were fitted in a linear model to obtain the displacement maps and confounders (G) in 8 interpolated cardiac phases across the 0 - 52.5% of the cardiac cycle.

2.3. Data acquisition

The Ethical Review Board (ERB) of the University Medical Center Utrecht approved the use of healthy volunteers for MRI protocol development. Nine healthy volunteers (6 males, 3 females, age 30 ± 4 years) were included and written informed consent was obtained in accordance with the ERB approval. The volunteers were scanned at 7T (Philips Healthcare, Best, The Netherlands) using a 32-channel receive head coil within an 8 channel transmit/receive head coil (Nova Medical) operated in quadrature mode. In each volunteer, 6 DENSE series with in-plane motion-encoding in the Right-to-Left (RL), Anterior-to-Posterior (AP) and Feet-to-Head (FH) direction were obtained. The series were acquired with different orientations: 2 sagittal series (in-plane FH and AP encoding), 2 coronal series (in-plane FH and RL encoding) and 2 transverse series (in-plane AP and RL encoding). The purpose of each of these DENSE series was to provide two components of the deformation gradient tensor (see Eq. (5) in Section 2.4.3), by taking the in-plane spatial derivatives from the motion encoded data (see Table S1 in the supplementary files for complete overview). Each DENSE series consisted of 72 slices and had the following imaging parameters (see Fig. 1): acquired resolution: $3 \times 3 \times 3\,mm^3$; FOV: $250 \times 250 \times 216\,mm^3$ (72 slices); multi-band factor: 3 (24 excitations); slice gap: 0 mm; displacement encoding (D_{enc}): 80 μm; 2 packages (12 excitations per package; odd slices in first package and even slices in the second); single-shot EPI readout (EPI factor: 33); SENSE factor: 2.6 (AP or RL, depending on acquisition orientation); TE/2: 20 ms and EPI band width in the readout/phase encoding direction; 2.7 kHz/pixel; 47 Hz/pixel. Furthermore, each DENSE series consisted of 24 repeated scans, in which 12 slice order permutations were applied together with 2 opposite encoding directions (to distinguish between motion-induced phase and phase confounders). Saturation effects from neighboring slices were remedied by acquiring odd and even slices in two separate packages. Slice order permutations for each repeated scan ensured that each slice was acquired at different time-locations into the cardiac cycle. Physiological data were simultaneously recorded by using a vector cardiogram (VCG) and a pulse oximeter (POx) for backup. Acquisition of each DENSE series had a duration of 48 heartbeats: 2 slice packages (odd vs. even slices; each package covering one cardiac interval) x 12 permutations over the cardiac cycle x 2 encoding polarities, resulting in a scan time of 48 s for 60 beats per minute (bpm) and 4:48 min total scan time to produce a complete set. Each slice package consisted of 12 slice groups, which, together with a MB factor of 3, resulting in 36 slices per cardiac interval. The temporal slice spacing depended on the heartrate of the volunteer and was chosen such that the 11 intervals between the 12 slices covered at least 50% of the cardiac cycle (which implies a temporal slice spacing of 45 ms for 60 bpm). The minimum temporal slice spacing required to perform the EPI acquisition was 42 ms, regardless of the heartrate. Furthermore, the time required between encoding and decoding the first slice was 30 ms, regardless of heart rate.

Time-resolved 2D CSF flow measurements were acquired using retrospectively-gated phase-contrast MRI (PCMRI) to compare the CSF stroke volume with the brain volumetric strain as an independent means for validation of the DENSE measurements. The 2D slice was planned at the C2-C3 level of the spinal canal. Motion-encoding was in the FH direction towards the spinal canal. Two different encoding sensitivities of 5 and 10 cm/s were acquired to obtain accurate measurements while avoiding phase wraps. Other imaging parameters included: acquired resolution $0.45 \times 0.45 \times 3\,mm^3$; FOV: $424 \times 408\ mm^2$; SENSE: 2 (RL) and 30 reconstructed cardiac phases over the cardiac interval. The scan duration of the PCMRI was 1:43 min for a heart rate of 60 bpm.

Two additional scans were acquired for data processing purposes. First, a T1-weighted (T1w) turbo field echo (TFE) scan (acquired resolution $1.00 \times 1.00 \times 1.00\,mm^3$; FOV $250 \times 250 \times 190\,mm^3$; TFE factor 600; inversion delay 1292 ms; SENSE 2 (AP direction); FA 5°; TR 4.2 ms; TE 1.97 ms; acquisition time 2 min) was acquired as anatomical reference. Second, two B0 field maps were obtained: the first was acquired at the beginning of the scanning session, and was used to perform second order image-based B0 shimming; the second was acquired after shimming to allow us to correct for remaining geometric distortions in the acquired DENSE images. A single B0 field map was reconstructed from the phase difference of two successive gradient echo scans with fixed TR, and different TE, as available from the vendor (acquired resolution $3.50 \times 3.50 \times 3.50\,mm^3$; FOV $224 \times 224 \times 224\,mm^3$; FA 8°; TR 3.9 ms; TE 1.57 ms and 2.57; scan duration: 25 s).

2.4. Strain tensor reconstruction

2.4.1. From dense series to displacement gradient fields

The acquired DENSE series were analyzed offline with custom software written in MATLAB R2018b (The MathWorks, Inc., Natrick, MA, USA). The positive and negative encoded slices in one DENSE series were registered using Elastix with a rigid transformation (Klein et al., 2010). Linear interpolation on the complex data was performed to transform the data. Since slices were acquired at different time-locations into the cardiac cycle, only in-plane translations and rotations were allowed during registration, preventing interpolation between adjacent slices that were not acquired at the same time location. The shimmed B0-map was then registered to the DENSE series and used for EPI distortion correction (Jezzard and Balaban, 1995). Registration and distortion corrections were applied to the real and imaginary components of the complex data of the DENSE series. After these initial corrections to the data, apparent displacement field maps were obtained from the phase signal for the positive and negative polarities of the encoding gradient (see Eq. (1)). These fields still included confounding factors from non-motion related phase contributions such as the RF phase. Gradients were derived from these apparent displacement field maps by computing spatial derivatives along the two in-plane coordinate axes. Each DENSE series thereby produced two apparent displacement gradient fields (which still contained phase confounders). As a result, 12 apparent displacement gradient fields for the 6 DENSE series were produced (see Supplementary Table S1). Phase wraps in the phase images caused a large numeric derivative $\Delta\varphi$, which was resolved by adding or subtracting 2π to $\Delta\varphi$ to bring it closer to zero if

$$|\Delta\varphi| > \Delta\varphi_{max} = 1.5\,\pi \tag{2}$$

which represents a maximum tolerated strain of

$$\varepsilon_{max} = \frac{\Delta\varphi_{max}}{2\Delta x}\frac{D_{enc}}{\pi} = \frac{3}{4}\frac{D_{enc}}{\Delta x} \tag{3}$$

For a resolution of 3 mm isotropic and an encoding sensitivity D_{enc} of 80 μm, this results in a maximum strain of 2%, which is well over the maximum expected tissue strains of 0.6%. The VCG and POx trigger data as recognized by the scanner software were used to deduce the positions of the acquired slices relative to the cardiac interval. Each apparent displacement gradient map was fitted voxel-wise to the physiological data in a linear model as described before (Sloots et al., 2020). To account for differences in heart rate between subjects, and between repeated scans, the linear model was defined for 8 cardiac phases at fixed relative positions in the cardiac cycle, in a way that is equivalent to linear interpolation between the 12 acquired heart phases. As a result, 8 displacement gradient maps were obtained, distributed over the over the cardiac cycle at 0, 7.5, 15, 22.5, 30, 37.5, 45 and 52.5% of the cardiac interval. The 8 displacement gradient maps over the cardiac cycle, show these displacement gradients with reference to end-diastole, which has by definition zero strain (and, thus, zero displacement gradients).

2.4.2. From displacement gradient fields to strain tensor

The displacement gradient fields were obtained from all 6 motion-encoded DENSE series that were acquired for each subject. Next, mag-

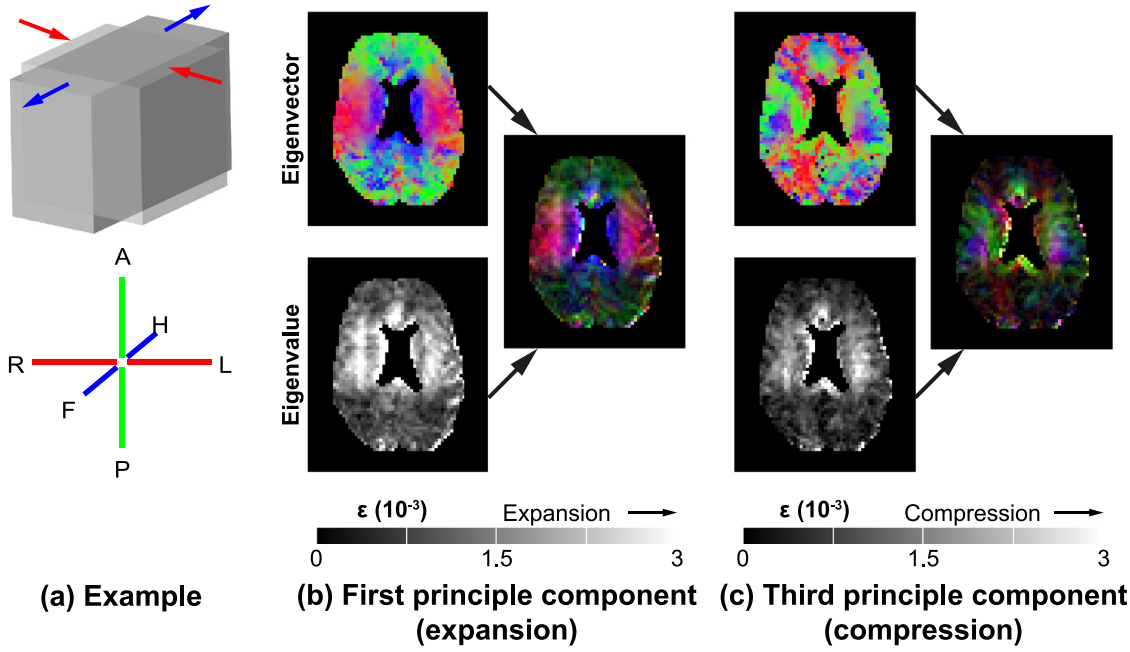

Fig. 2. (a) Top figure: A deformed voxel at peak systole relative to end-diastole serves as an example to illustrate how a voxel stretches along a certain 1D direction (blue arrows), while at the same time it compresses along another orthogonal direction (red arrows). Bottom figure: The RGB color coding of directionality (Pajevic and Pierpaoli, 1999). Red: Right-to-Left (RL); green: Anterior-to-Posterior (AP) and blue: Feet-to-Head (FH). Figure b and c show the direction and magnitude of largest expansion (first principal strain) and largest compression (third principal strain) in each voxel for subject 4, respectively (unsmoothed data from measurement 1 in its native space). Top figure: the direction of the eigenvector in each voxel using the directionally encoded color scheme. Bottom figure: gray-scale maps representing the magnitude of the associated principle strain. For the third principle component, the absolute value of the eigenvalues was taken, resulting in a map with only positive values. Multiplying the eigenvectors with the eigenvalues results in an intensity color map.

nitude data of these DENSE series were used to register the displacement gradient fields by using Elastix in a group-wise rigid registration in combination with third order b-spline interpolation (Klein et al., 2010). Each DENSE series provided two components of the displacement gradient tensor. For instance, the sagittal oriented dataset with FH encoding direction from Fig. 1 provides the displacement gradient fields $\frac{\partial u_{FH}}{\partial FH}$ and $\frac{\partial u_{FH}}{\partial AP}$ (see Eq. (5)). The diagonal elements of the displacement gradient tensor were obtained twice, each for a different acquisition orientation. We inspected the consistency between the pairs of diagonal elements and confirmed that they showed reasonable agreement and no systematic differences (see Figure S3 in the supplementary files for consistency). Hence, we averaged the pairs of data before the strain tensor was obtained from Eq. (4). In this work, we reconstructed the strain tensor of tissue relative to diastole (e.g. the R-top in the ECG signal). The strain tensor describes the stretch and compression behavior of an image-voxel along three orthogonal directions. In principle this can be any direction, yet, for three dimensions, the eigenvalue decomposition returns the three directions in which only pure stretch or compression occurs, without shear strains. The accompanying eigenvalues are the respective strains in these directions, and known as the principal strains. We will mainly focus on two of these directions: the first principle direction of dominant stretch and the third principle direction of dominant compression. The principle strains are visualized by using directionally encoded color (DEC), known from diffusion tensor imaging, enabling qualitative visual comparisons (Pajevic and Pierpaoli, 1999). Fig. 2 shows this principle, where the direction of the eigenvector in each voxel is depicted by the RGB color scheme, while the intensity represents the magnitude of associated principle strain.

2.4.3. Volumetric strain and octahedral shear strain

The Lagrangian strain tensor strain tensor **E** can be written as follows [31]:

$$\mathbf{E} = \frac{1}{2}\left(\mathbf{F}^{\mathbf{T}}\mathbf{F} - \mathbf{I}\right) = \begin{pmatrix} \varepsilon_{xx} & \varepsilon_{xy} & \varepsilon_{xz} \\ \varepsilon_{yx} & \varepsilon_{yy} & \varepsilon_{yz} \\ \varepsilon_{zx} & \varepsilon_{zy} & \varepsilon_{zz} \end{pmatrix} \quad (4)$$

E is symmetric and independent of rigid body translation or rotation. It describes the tissue deformation, where the diagonal elements of **E** (ε_{xx}, ε_{yy} and ε_{zz}) describe the local stretch (positive) or shortening (negative) of the tissue in the associated direction, while the off-diagonal elements describe the shear components. The deformation gradient tensor **F** is given by

$$\mathbf{F} = \nabla\mathbf{u} + \mathbf{I} \quad (5)$$

where **I** is the identity matrix and u_x, u_y and u_z are the measured displacements in Right-to-Left, Anterior-to-Posterior and Feet-to-Head, respectively. From **E** we derive two scalar quantities: the volumetric strain and octahedral shear strain. The volumetric strain reflects net expansion or compression of the voxel, relative to (in the present study) end-diastole. Under the assumption of very small deformations, the volumetric strain ε_V can be approximated by summing over all eigenvalues[12]:

$$\varepsilon_V = \frac{\Delta V}{V} \approx \varepsilon_{xx} + \varepsilon_{yy} + \varepsilon_{zz} \quad (6)$$

Octahedral shear strain signifies how much the voxel deforms and is independent of volumetric strain. The octahedral shear strain can be considered as a measure for the differences between of the three principal strains, indicating the deviation from isotropic swelling (three equal, positive principal strains) of a voxel during the heartbeat and is given by Eq. (7) below (McGarry et al., 2011).

$$\varepsilon_S = \frac{2}{3}\sqrt{\left(\varepsilon_{xx} - \varepsilon_{yy}\right)^2 + \left(\varepsilon_{xx} - \varepsilon_{zz}\right)^2 + \left(\varepsilon_{yy} - \varepsilon_{zz}\right)^2 + 6\left(\varepsilon_{xy}^2 + \varepsilon_{xz}^2 + \varepsilon_{yz}^2\right)} \quad (7)$$

While the octahedral shear strain is zero for isotropic swelling (or shrinkage), it is larger than zero for deformations (either isovolumic or non-isovolumic) with different principal strains (e.g. stretch in one direction and compression in a perpendicular direction). The octahedral shear strain is a positive number, while a value of 0 indicates isotropic deformation of the voxel (i.e. the same amount of stretch or compression in each orthogonal direction).

2.5. Repeatability

DENSE series were repeated with repositioning of the subject to assess the test-retest reliability of the measurements. The total scan session including both repeated measurements lasted less than 90 min. Comparing the original measurement with the repeated measurement was done by rigid registration of the T1w scan associated with the repeated measurement to the T1w scan associated to the original dataset. The resulting transformation was then performed on the displacement gradient fields belonging to the repeated measure using third order b-spline interpolation. Both T1w scans were segmented using Computational Anatomy Toolbox (CAT12, version 1615, Jena University Hospital, Departments of Psychiatru and Neurology) for Statistical Parametric Mapping (SPM12, version 7771, Wellcome Trust centre for Neuroimaging, University College London) and a combined brain mask was created out of the tissue probability maps, where voxels containing any CSF in the original or the repeated T1w scan were discarded. An additional city-block erosion step was included to assure that no partial volume effects from CSF were present in the deformation gradient maps, as neighboring voxels would influence values in a given voxel via the derivative calculations. All remaining voxels were used to assess regional repeatability.

Per subject, repeatability analysis was performed on the eigenvalues, volumetric strain and octahedral shear strain measures deduced from the two strain tensor reconstructions. The analysis was separately performed for seven brain regions of interest (ROIs): cerebellum, brain stem, basal ganglia, temporal lobe, occipital lobe, parietal lobe and frontal lobe. MNI labels registered to the original T1w scan were used to distinguish between the different regions. The repeated measurements were evaluated using the voxel-wise SNR as the reciprocal of the coefficient of variation:

$$SNR = \frac{|\mu|}{\sigma} \tag{8}$$

where μ is the mean of the two measurements averaged over all voxels in the ROI and σ the standard deviation over the voxel-wise difference between the measurements.

2.6. External validation

Per subject, the volumetric strain measurements were validated against the CSF in/outflow in the foramen magnum. To this end, we compared the average volume change of brain tissue resulting from the volumetric strain to the change in CSF volume obtained at the C2-C3. This method was used previously to validate the multi-shot 3D DENSE method and an approximately linear relationship was reported between CSF flows and brain tissue volume pulsations over the cardiac cycle (Adams et al., 2020). Here we use the same approach to validate the current single-shot SMS DENSE method.

The average volume change over the cardiac cycle can be obtained from the whole-brain average volumetric strain by solving Eq. (6) for ΔV. The absolute volume of white matter and gray matter was obtained through brain segmentation of the T1w scan (registered to the mean DENSE magnitude image resulting from the group-wise registration) using CAT12. From the tissue probability maps, a mask was created where all voxels containing any CSF in the original or the repeated T1w scan were discarded. An additional city-block erosion step was included to assure that no partial volume effects from CSF were present. This way, the analysis was exclusively due to the rise in volume of the tissue, as all CSF and large vessels embedded in the CSF, like the circle of Willis, were excluded by using such a stringent mask. The average volumetric strain was obtained over the same eroded, CSF free tissue mask, that was generated for assessing the regional repeatability. Multiplying the volume of grey and white matter with the average volumetric strain, resulted in the volume change over the cardiac phases.

The volume of CSF was calculated by integrating the CSF velocity maps over the cardiac cycle and multiplying the result by the area of the spinal canal. Furthermore, the volume curves were shifted in time to compensate for the encoding delay in the DENSE series. The encoding delay is defined as the time between an observed R-top trigger by the MRI system and the encoding gradient applied to encode the signal. The encoding delay was 20 ms, resulting in a shift of 2–3%, depending on the heartrate. Both the tissue volume curve and CSF stroke volume curve were independently corrected so that they both would intersect the origin at point (0, 0).

2.7. Average strain tensor

The overall behavior of the strain tensor was assessed by combining the results of the first measurement for all individual subjects in MNI space (ICBM 2009c Nonlinear Symmetric Fonov et al., 2009, Fonov et al., 2011). Per subject, the reconstructed strain tensor was registered to MNI space using the associated T1w scan: First, the T1w scan was registered to the mean DENSE magnitude image resulting from the group-wise registration of the six DENSE series, after which it was registered to MNI space by using Elastix using an affine registration followed by a non-linear b-spline regularized registration (Klein et al., 2010). The resulting transformation was then applied to the strain tensor with third order b-spline interpolation for the eigenvalues and nearest neighbor interpolation for the (unit) eigenvectors. Furthermore, the direction of the eigenvectors were corrected using the rotation component of the affine registration step (Leemans and Jones, 2009). The volumetric strain and octahedral shear strain were computed in native space before transforming the maps to MNI space. Third order b-spline interpolation was used when transforming these scalar maps to MNI space. The resulting maps were averaged over all subjects, resulting in average maps for the first eigenvector (most expansion), the third eigenvector (most compression), the volumetric strain and octahedral shear strain. SNR maps representing the voxel-wise SNR derived from the repeated measurements, were also included for the volumetric strain and octahedral shear strain (see Eqs. (6) and (7).

3. Results

3.1. Strain tensor

Fig. 2 represents an example of the strain tensor map for subject 4 at peak systole (specifically 30% of the cardiac cycle for the current subject) in the native space of this subject. Only the first principal strain (maximum expansion, Fig. 2b) and third principle strain (maximum compression, Fig. 2c) are represented together with its associated eigenvalue. In rare occasions an eigenvector decomposition of a voxel resulted in either three positive (< 1% of the voxels) or three negative eigenvalues (< 0.3% of the voxels). In these cases respectively, the associated compression (third component) or expansion direction (first component) were set to 0. The first principle strain and third principle strain will be referred to as the positive strain and negative strain, respectively.

Brain regions with large expansions (positive strain) were generally accompanied by large compressions (negative strain) in a direction perpendicular to the expansion direction. This observation, where axial expansion of an object in the direction of the expansion load is accompanied by transverse compression, is also known as the Poisson effect (See Fig. 2).

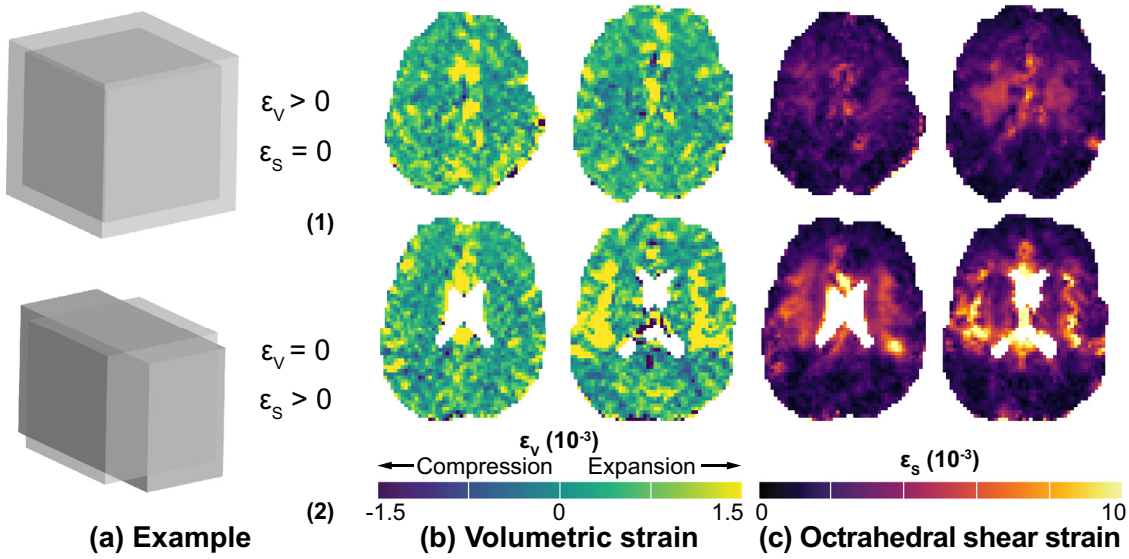

Fig. 3. Volumetric strain and octahedral shear strain for subject 5 (unsmoothed data from measurement 1). (a) Example demonstrating the concepts of volumetric strain and shear strain. The first example (top) shows a voxel with isotropic swelling at peak systole. This voxel increases its volumetric strain without inducing shear strain. The second example (bottom) represents a voxel with isovolumic deformation (preserving its volume), which yields non-zero octahedral shear strain (McGarry et al., 2011). (b) Peak volumetric strain (with respect to diastole) shows an increase at the cortical surface and near sulci. (c) Peak shear strain is most pronounced in regions near the ventricles. The volumetric strain and octahedral shear strain barely correlate ($R^2 < 0.0001$ for current subject), illustrating that they reflect different aspects of the deformation of the voxel.

3.2. Volumetric strain and octahedral shear strain

Peak systole, defined as the moment of largest mean volumetric strain, ranged between 30 and 37.5% of the cardiac interval, depending on the subject. Fig. 3 shows the volumetric strain and octahedral shear strain at peak systole for subject 5 at different locations in the brain. Cortical regions show mostly isotropic expansion (low shear strain). Volumetric strain and shear strain did not substantially correlate (average $R^2 = 0.003$). On average, peak volumetric strain and peak shear strain were reached at the same time. However, in subject 5 the volumetric strain peak came after the peak in octahedral shear strain, at 37.5% and 22.5%, respectively. This observation was consistent between the first and repeated scan.

3.3. Per subject

The individual strain maps are provided in Fig. 4 for all subjects. The results show similar trends for all subjects, where the positive principal strain direction follows the known brain motion pattern, which is funnel shaped and pointing towards the foramen magnum (Greitz et al., 1992). The negative principal strain direction is somewhat heterogeneous across subjects, but its magnitude correlates with the magnitude of the positive principal strain, reflecting the Poisson effect in all subjects. The volumetric strain is larger in regions where more gray matter is present. On the other hand, the octahedral shear strain is more pronounced in regions in the white matter, near the ventricles. Data quality was high in all subjects with some visible artifacts (stripes) in subject 3 and 6, presumably due to subject motion during scanning.

3.4. Repeatability

Repeated measurements were performed for all subjects, except subject 3, who opted out after the first scan as he felt uncomfortable. Subject 3 could therefore not be included in the repeatability study.

The comparison between the initial measurement and the repeated measurement is shown in Fig. 5, which consists of a summarized Bland-Altman plot for each individual subject, for seven spatial brain regions. The mean of the two repeated scans is shown as a black dot, with surrounding error bars representing the non-parametric reproducibility coefficient (+/- 1.45 · interquartile range). The mean voxel-wise SNR (see Eq. (8)) over all subjects per ROI is presented as well. The complete set of Bland-Altman plots for the volumetric strain and octahedral shear strain of one of the subjects, is shown in the supplementary files (see Figure S4 and S5).

Of the quantities that were assessed, the octahedral shear strain shows the best voxel-wise repeatability and also has the highest SNR in all regions compared to the other quantities. Volumetric strain has the lowest SNR and showed poor voxel-wise repeatability.

3.5. External validation

A good agreement was found between volumetric tissue strains and the changes in the CSF flow through the spinal canal over the cardiac cycle, between 0 and 52.5% (see Fig. 6). Linear regression of volumetric tissue strain versus CSF yielded a mean slope of 0.78 ± 0.10 with R^2 of 0.91 ± 0.08. The peak CSF stroke volume occurred at 43% of the cardiac interval and was on average 0.58 mL ± 0.09 mL. The peak in brain tissue volume increase was on average 0.46 mL ± 0.11 mL and occurred at 34% of the cardiac interval.

3.6. Average strain

The overall behavior of the strain tensor, volumetric strain and octahedral shear strain in MNI space, averaged across subjects, is shown in Fig. 7. This figure clearly shows distinct strain patterns. These patterns are already discernable at the individual subject level in Fig. 4, but can be better explored in relation to brain anatomy on the averaged data. While tissue expansion roughly follows the typical macroscopic, funnel-like direction towards the foramen magnum, some white matter bundles can be distinguished due to a different expansion direction compared to its surroundings. The location that might be the corona radiata (Ahn and Lee, 2011), for example, has a different expansion direction

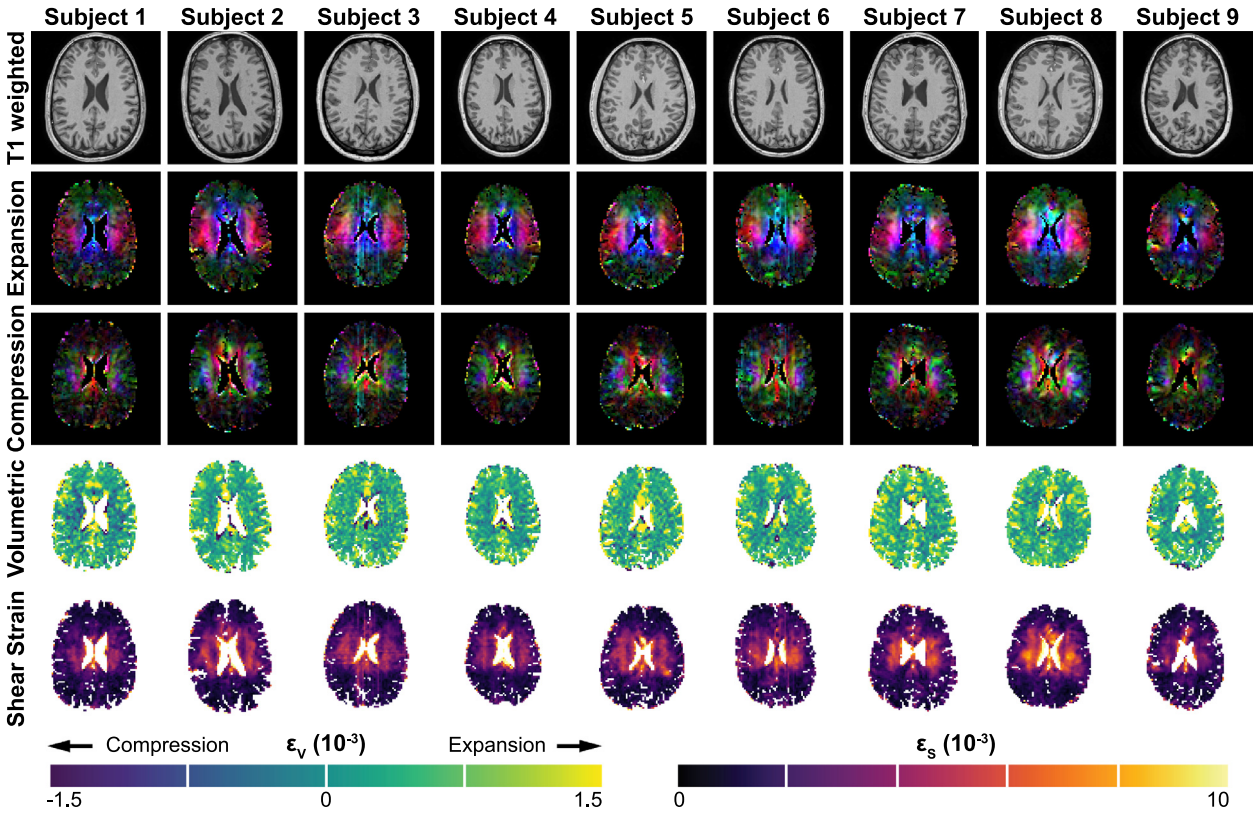

Fig. 4. Transverse slice in the middle of the brain represented for each subject (columns) and the various outputs from the strain tensor analysis (rows). The color scaling of the principle strains is the same as illustrated in Fig. 2. The T1-weighted image is shown as anatomical reference (top row). A similar trend in all subjects can be observed. The positive principal strain tensor (second top row, expansion) follows the known funnel shaped pattern pointed towards the foramen magnum (Greitz et al., 1992). The negative principal strain tensor (middle row, compression) is more heterogeneous across subjects, but is locally of the same magnitude as the positive principal strain, reflecting the Poisson effect. The volumetric strain (second bottom row) is larger towards the periphery of the brain compared to regions where white matter is present. Furthermore, the volumetric strain is weakly correlated to the octahedral shear strain (bottom row), which shows large shear strains in the white matter, around the ventricles.

compared to its surrounding white matter tissue (see Fig. 7). The same fiber tract is also observed in the octahedral shear strain, where this bundle has reduced anisotropy compared to its surrounding. Furthermore, tracts like the cerebral peduncles and corpus callosum also show distinct expansion from surrounding tissue, which is accompanied by large shear strains. The rostral slices indicate increased shear strain in the deep white matter structures (i.e. centrum semiovale and cingulum) relative to the cortical gray matter.

Volumetric strain, on the other hand, is most pronounced at the cortical gray matter and basal ganglia. Here, it should be noted that the mask overlaying the results was derived from the CSF probability map, but did not include an additional erosion step to assure no partial volume effects from CSF. As a result, regions adjacent to CSF (e.g. ventricles or sulci) may suffer from artefacts due to free moving water. This is reflected by extreme values in these areas, especially visible in the volumetric strain map, and is shown in more detail in the supplementary files (Figure S6). Voxel-wise SNR maps of the volumetric strain and octahedral shear strain are added to the figure in the bottom two rows, where the standard deviation was calculated over the nine subjects. The average SNR across voxels for the volumetric strain and shear strain in the brain's tissue was 0.82 and 3.4, respectively. Again, virtually no correlation between volumetric strain and octahedral shear strain was found ($R^2 = 0.0004$).

4. Discussion

In this work, we presented a comprehensive single-shot DENSE sequence that combines the benefit of sufficient SNR to perform a voxel-wise strain analysis, with a simultaneous multi-slice acquisition approach that enables whole-brain coverage within approximately 5 min of scan time. We used the developed sequence to reconstruct the strain tensor of brain tissue resulting from cardiac pulsations in the microvasculature and explored its behavior across the brain (Soellinger et al., 2009, Adams et al., 2020, Adams et al., 2019). Additionally, we derived two scalar maps: volumetric strain and octahedral shear strain. We acquired the strain tensor in nine subjects, with repeated measurements in eight subjects to assess test-retest reliability. An external validation of the volumetric strain was performed by correlating the results to the CSF flow at the C2-C3 level. By combining the data from all subjects to MNI space, we documented the behavior of tissue deformation as for an average brain and investigated the inter-subject consistency of the observations. To the best of our knowledge, this is the first time that the full strain tensor from cardiac-induced deformation is measured in the human brain with full brain coverage.

The cardiac-induced 3D strain tensor was visually represented by the first principle strain (expansion) and third principle strain (compression). These deformation maps reflect neuroanatomical details of the brain's structure; parts of white matter bundles like the cerebral peduncles, corpus callosum and corona radiata in the centrum semiovale can be distinguished due to a different expansion direction compared to their surrounding tissue. Regions with large positive eigenvalues, often show large negative eigenvalues as well, reflecting the Poisson effect. Given the random orientation of the microvasculature, we initially expected a more isotropic deformation pattern (less shear strains) as a result of the non-oriented swelling of the microvascular bed. However, the first

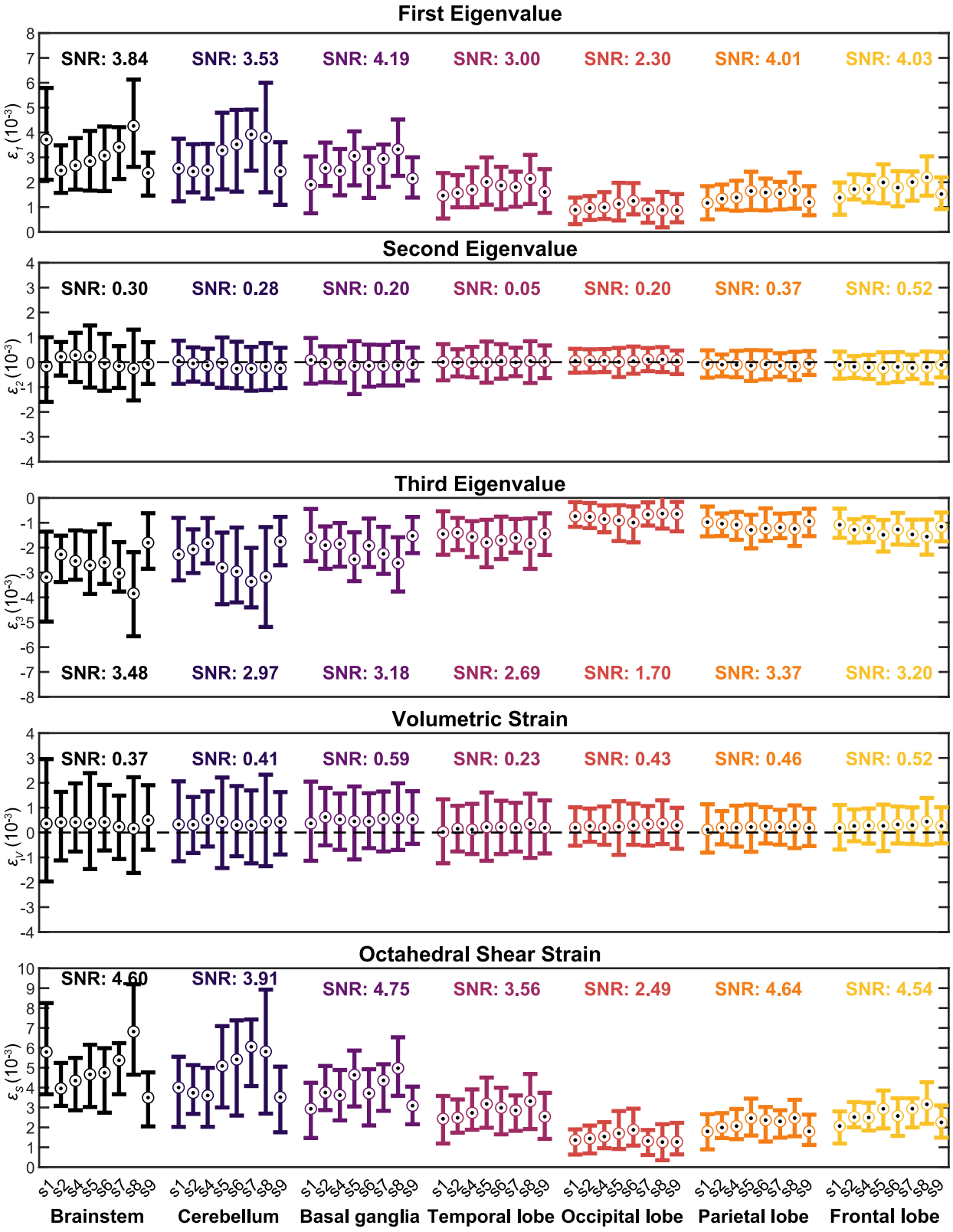

Fig. 5. Representation of the voxel-wise analysis of the repeated measurements for seven separate brain regions. Each error bar in fact represents a summarized Bland-Altman plot of one subject for each brain region (see Figure S4 and S5 for complete Bland-Altman plots). The mean of the two repeated scans is shown as a black dot. The reproducibility coefficient and systematic offset from the voxel-wise difference between the two scans in the indicated brain region are indicated as follows: the error bar represents the non-parametric reproducibility coefficient (+/- 1.45 · IQR) and systematic offset is captured by a shift of the error bars with respect to the mean. As a result, repeated measurements without a systematic difference have a positive and negative error bar of equal length. The systematic offset between the two scans was at most $0.4{\cdot}10^{-3}$ for the octahedral shear strain and $0.2{\cdot}10^{-3}$ for the volumetric strain. The listed SNRs represent the SNR within each brain region derived from the voxel-wise difference between the repeated scans (see Eq. (8)), averaged over all subjects.

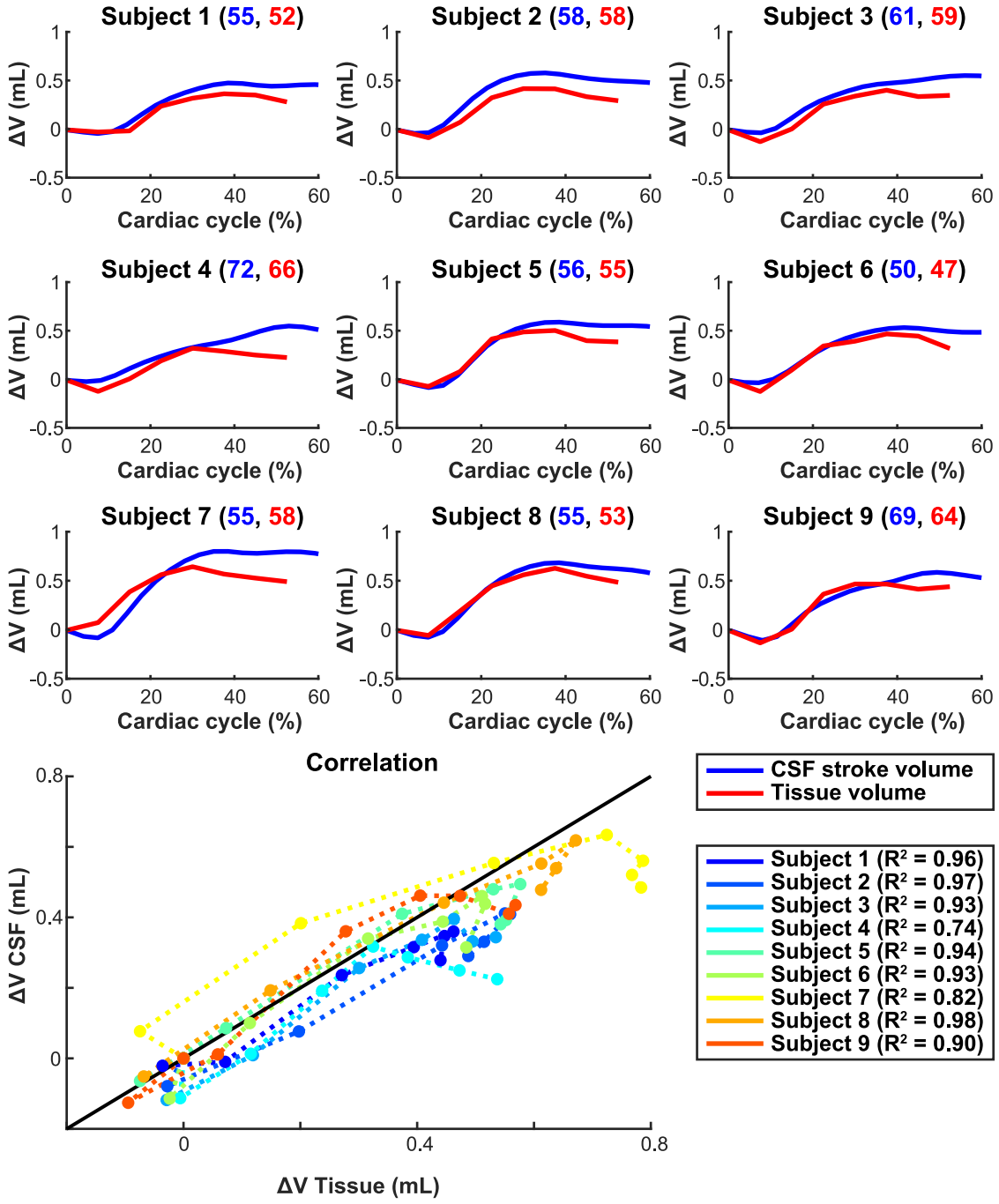

Fig. 6. Per subject comparison of CSF volume expelled from the intracranium (measured at the C2-C3 level) with tissue volume change obtained from the volumetric strain measurements. The expelled CSF volume (in mL) is shown over the cardiac cycle interval running from 0 to 60%. Tissue volume measurements were obtained only for 0 to 52.5% of the cardiac interval. Numbers in the title of each graph represent the average heartrate of the subject for the associated measurements (CSF stroke volume in blue and tissue volume in red, in beats per minute). Additionally, we provide a correlation graph that shows the relation between expelled CSF volume and tissue volume change. Each subject is represented by a different colored line; the black line indicates the identity relation.

principle strain is predominantly directed both towards the ventricles and downwards towards the brain stem, which could reflect low resistance towards CSF spaces. We found principle strains ranging from 0.09 – 0.43% (Fig. 5), with largest strains in the brain stem (range: 0.23% – 0.43%) and lowest strains in the occipital lobe (range: 0.09% – 0.12%), indicating regional heterogeneity of tissue deformation. Pahlavian et al. mention 0.38% as maximum principle strain observed in the brain stem (Pahlavian et al., 2018, Spottiswoode et al., 2007)which compares well to our findings. Yet, they derived **F** under the assumption of volume conservation, which relies on the false assumption of no volumetric strain fluctuations (Hirsch et al., 2013, Adams et al., 2019, Sloots et al., 2019). As a result, it is necessary to measure **F** in all directions. Furthermore, it is not directly apparent to what extent regional microstructure affects the strain tensor's behavior. While tissue expansion roughly follows the typical directions of white matter fiber bundles pointing towards the foramen magnum, the corpus callosum, for example, mainly expands in directions perpendicular to the fiber bundles running from the left to right hemisphere (Basser et al., 1994, Mori et al., 1999). It should be noted that we implicitly assumed that the strain tensor would not change principal directions during the cardiac cycle, so we could limit

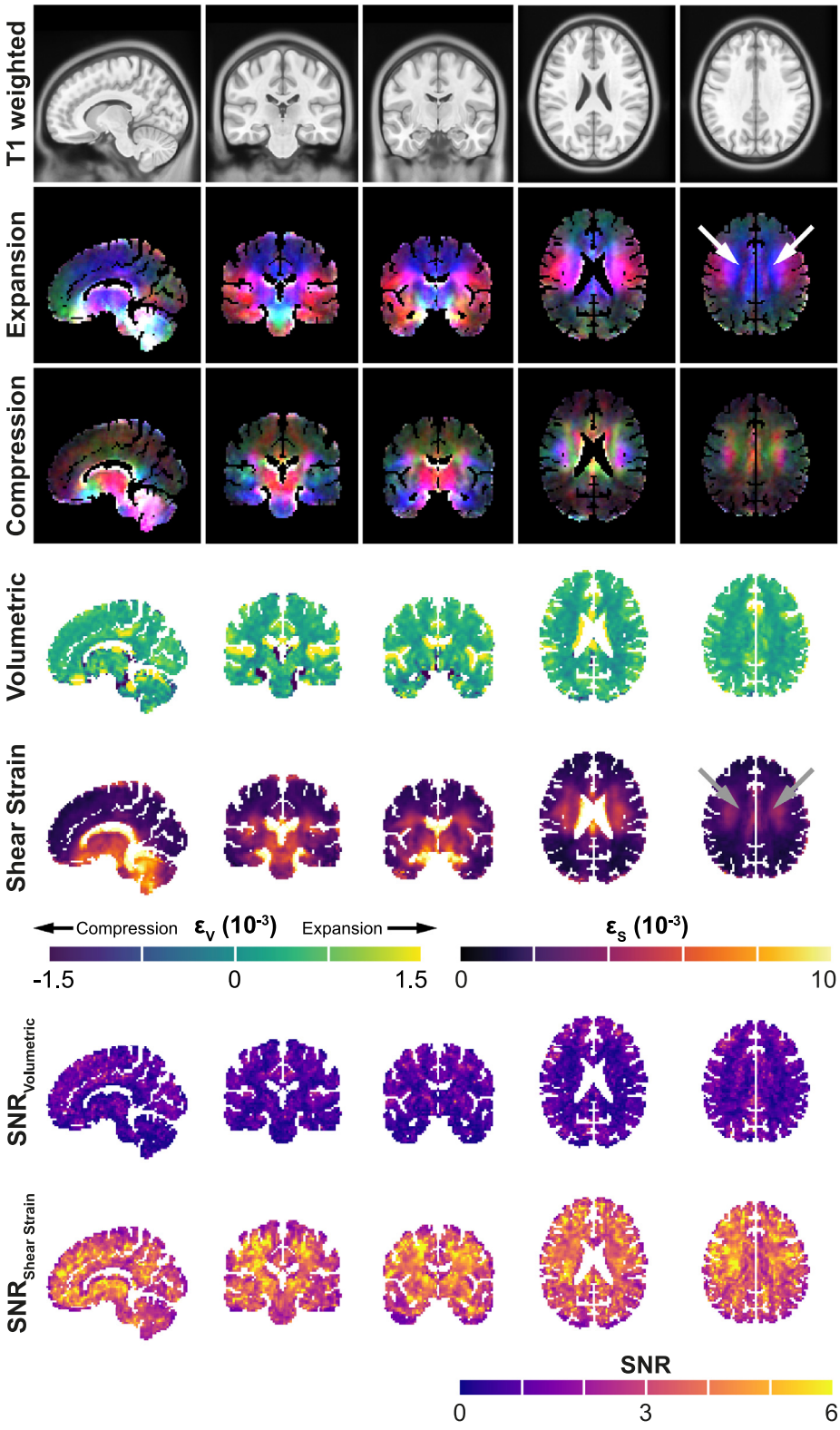

Fig. 7. Voxel-wise average of the positive and negative strain in MNI space over all 9 subjects (taking measurement 1 only, without smoothing of the data). A T1-weighted image is included for anatomical reference. The voxel-wise average of the volumetric strain and octahedral shear strain are shown as well, including an SNR map of the volumetric strain and shear strain, where the standard deviation per voxel was calculated over the nine subjects in MNI space. Color scaling for the positive and negative principle strain is different from Fig. 2 and is limited to $2{\cdot}10^{-3}$ to better capture the anterior and posterior structures. Color scaling for the volumetric strain and shear strain is equal to the scaling presented in Fig. 3. Please note that voxels adjacent to CSF may suffer from artefacts due to free moving water. Especially the extreme values in the volumetric strain maps are probably artefacts due to partial volume effects. The figure shows how specific tracts and other anatomical structures clearly emerge from the strain maps, with distinct patters for different adjacent structures. The bundle that looks like the corona radiata, for example, can be distinguished due to a different expansion direction compared to its surrounding white matter tissue and is indicated with white arrows (expansion map), and a lower octahedral shear strain, as indicated with gray arrows (anisotropy map).

our analysis to the strain tensor at peak systole. The exact time course of the strain tensor over the cardiac cycle and its relation to the microstructure of the brain remain topics for future research.

The different locations for which volumetric strain and shear strain are most pronounced, show that these quantities depict different aspects of the local mechanical behavior of the tissue. Especially shear strain showed good repeatability and relative high SNR. Volumetric strain, on the other hand, was most difficult to repeat on a voxel by voxel basis. This is due to the summation over all three eigenvalues, of which the first (positive) and the last (negative) eigenvalues largely cancel each

other, while the noise increases by a factor of $\sqrt{3}$ from the summation. Yet, averaging over a small ROI already leads to enough noise reduction to detect regional physiological differences reflected by the volumetric strain. For instance, individual volumetric strain maps already show regional differences in subjects between the insula and white matter. Comparing the SNR to previous work shows that we gained at least a factor of 1.8 in SNR of the volumetric strain maps[12]: Adams et al. reported a voxel-wise standard deviation of the volumetric strain of $1.4{\cdot}10^{-3}$, while we measured an SNR for strain of 0.39 (mean over all regions), which corresponds to a standard deviation of $0.74{\cdot}10^{-3}$ (given an average volumetric strain of $2.9{\cdot}10^{-4}$). In comparing these numbers one should note that Adams' estimation was theoretically derived from SNR measurements of the magnitude images, while we obtained the noise estimate from voxel-wise comparison between repeated scans after repositioning. Our noise estimation, thus, includes contributions from physiological noise and imperfections in the registration. Most importantly, the 3D approach used by Adams et al. often suffered from increasing artifact levels towards the end of the cardiac cycle due to inter-shot phase inconsistencies, which we avoided by the single-shot approach. These artifacts cannot easily be quantified and prohibits in depth comparison of the gain in SNR and image quality. Nevertheless, we obtained the gain in SNR in less than half of the scan time (4.8 min vs 13.5 min), albeit at the cost of an increased voxel size (3 mm versus 2.2 mm isotropic resolution).

The rise in blood volume that enters the cranium from the heart during systole, is compensated by an outflow of CSF into the spinal canal. We measured the cerebral tissue expansion with DENSE and assessed the outflow of CSF at the C2-C3 level. Given the incompressibility of CSF, this approach is justified under the Monro-Kellie doctrine, which implies a fixed intracranial volume (Greitz et al., 1992). We analyzed the 0–50% cardiac interval and found an approximate linear relationship between CSF and volumetric strain over the cardiac cycle, which is consistent with current concepts of intracranial volume change (Adams et al., 2020). Since the phase difference between the two curves is known to be minimal, no additional challenges were posed on this analysis (Adams et al., 2020). Yet, the method does not take into account contributions from both larger arteries and veins embedded in the intracranial CSF. The C2-C3 location is often used to measure CSF outflow, since the narrow spaces ensure higher and more homogeneous flows, mainly directed Feet-to-Head, which can be measured more reliably (Greitz et al., 1992, Balédent et al., 2004, Alperin et al., 2005). The choice of this location by us and in previous literature, implicitly assumes that CSF volume buffering between the foramen magnum and this level is negligible compared to the volume buffered by the rest of the spinal sac below the C2-C3 level, which seems reasonable given the relative proximity to the foramen magnum. The internal validation of our method with CSF stroke volumes confirms the correct implementation and scaling of the strain measurements obtained through DENSE. The effect on volumetric strain due to partial volume effects was addressed by including a stringent mask to calculate the volumetric strain. Still, it remains a limitation of this method that we could assess the DENSE series only with a rather coarse resolution of 3 mm isotropic. The effective resolution of the derived strains is further reduced by the spatial derivative operation, which uses the displacement information from two neighboring voxels to compute the strain. These artifacts are particularly seen at CSF-tissue boundaries as shown in Figure S6, and also visible around the ventricles of other work (e.g. Fig. 2 in reference Pahlavian et al., 2018). We mitigated these effects as much as possible by using a stringent mask. Computing the derivative on the complex signal through the Fourier transform could possibly avoid smoothing through the spatial derivative, albeit at even higher noise amplification than the spatial derivative operation (De Leeuw and Bakker, 2012). Nevertheless, we are hampered in our analysis by partial volume effects, especially in regions near free moving water like sulci, and in structures that fall below the current resolution, like the cerebral cortex. Cortical regions tend to contribute more to the average volumetric strain compared to the deep white matter structures. Excluding these voxels from the analysis by the stringent masking, probably led to a slight underestimation of the tissue volume compared to the CSF. Although the ability to study the swelling of the microvasculature bed with DENSE remains advantageous over 'mass-balance' approaches that study blood- and CSF flows at the spinal canal (Balédent et al., 2004, Wåhlin et al., 2012), the proposed method has currently limited capabilities to avoid partial volume effects with medium- to large-sized vessels at the cortex, which may hamper accurate assessment of cortical gray matter volumetric strains. In the meantime, the rather good correlation between CSF flows and total brain tissue volumetric strain shows the potential of 2D CSF measurements at the spinal canal as a straightforward approach to assess the average pulation of the brain's blood volume. Since CSF measurements are easily done and have less SNR constraints, it may be attractive to perform these measurements at 1.5 or 3T (Balédent, 2012). One caveat, however, is the open question whether it will faithfully reflect cerebral blood volume pulsations in disease, as the relative contribution from the vessels embedded in the brain tissue and the larger vessels in the CSF might be different in disease.

The DENSE method has some intrinsic properties that are important to consider when comparing DENSE with other methods (e.g. PC-MRI) or for different field strengths. The stimulated echo acquisition employed by DENSE ensures that signal loss during the time between encoding and decoding is predominantly proportional to T1, and decays with T2 as function of the TE (Frahm et al., 1985). As a result, the time between encoding and decoding can be extended significantly with DENSE compared to PC-MRI, resulting in increased motion sensitivity (Weaver et al., 2012). Besides, tissue T1 time-constants are considerably longer at higher field strengths, yielding a better performance of this sequence at high-field for longer encoding-decoding delays. When optimizing the DENSE motion sensitivity for assessing strain like we did in the current paper, the largest source of signal loss is due to diffusion effects arising from the large b-values induced by the large encoding gradients combined with long decoding times, which does not change with field strength. In studies that used DENSE for tissue displacement only, diffusion effects did not play a key role since the encoding sensitivity (and thus the associated b-value of the encoding gradients) was limited to avoid phase wraps (Soellinger et al., 2009, Zhong et al., 2009). In this study, the high sensitivity of the DENSE sequence resulted in raw displacement images corrupted with many phase wraps, which prohibits the reconstruction of displacement images. Furthermore, the high sensitivity of the sequence prohibits the use of a multi-shot approach to potentially increase the resolution. Phase inconsistencies between shots from involuntary subject motion may then lead to artifacts. While we mitigated this effect by using a single-shot approach, we are limited in the spatial resolution. Furthermore, we do not think the proposed method can tolerate a 3/7 factor reduction in SNR resulting from a translation to 3T clinical scanners without compensating this SNR loss by, for example, further increasing the voxel size.

Volumetric strain reflects both blood volume increase (microvascular expansion) and tissue stiffness. For instance, white matter could be stiffer (Jin et al., 2013) and has reduced blood-volume to tissue ratio compared to gray matter (Bulte et al., 2007, Vonken et al., 1999, Artzi et al., 2015). These combined properties result in volumetric strain increase being dominant in the cortical gray matter compared to white matter regions. Extensive elastography reconstructions could help to unravel blood volume change from tissue elasticity (Tan et al., 2017), providing a window to tissue integrity as well as perfusion pressure (Hetzer et al., 2018). Yet, it is important to note that, besides microvascular expansion and tissue stiffness, the volumetric strain also reflects potential simultaneous compression of the interstitial space and draining veins that act as Starling resistors (DE Simone et al., 2017). Comprehensive computer models that take into account the interaction between blood and CSF, while correcting for tissue stiffness, could help to gain further insight into these effects (Linninger et al., 2005, Linninger et al., 2009, Sack et al., 2011). In the meantime, the observed volumetric tis-

sue strain can be regarded as a lower bound estimation of the underlying blood volume pulsations and may help in advancing our understanding of diseases like cerebral small vessel disease and vascular contributions to neurodegenerative diseases (Sloots et al., 2020).

The mean spatial pattern of high octahedral shear strain roughly follows the distribution of deep medullary veins as reported previously (Kuijf et al., 2016). The presence of these medullary veins may reduce the apparent shear stiffness of these regions. The deep medullary veins support the venous drainage of the brain and have shown abnormalities in the context of different cerebrovascular diseases (De Guio et al., 2014, Yan et al., 2014, Mucke et al., 2015). Although the current young population is not a representative group to study these types of diseases, these results show that the technique is sensitive enough to detect regional normal differences in tissue deformation that can be compared with other structural brain maps. This indicates that the technique has potential for studying abnormal tissue deformation in disease.

The technique proposed in this study is prone to EPI distortion. To mitigate the effects, we used 2nd order image-based B0 shimming. To address remaining geometric distortions, we used a shimmed B0 field map to correct these. Registration to a reference volume or blip-up blip-down acquisition are alternative methods that aim to solve EPI distortion corrections, and are in principle suited to implement as an alternative (Andersson et al., 2003) Since the spatial derivative used to obtain strain maps depends on an accurate distance between adjacent voxels, it is important to correct for EPI distortions before the strain is computed from the displacement fields. Moreover, the different acquisition orientations also require correct EPI distortion correction, especially as they do not all share the same phase encoding direction. Here, it must be acknowledged that the correction and registration steps used in this method are prone to error propagation due to multiple interpolation steps. Although we tried to mitigate these effects by linear interpolation on the complex data and limited degrees of deformation freedom in the groupwise registration, especially the MNI registration may have induced additional noise. Furthermore, it should be mentioned that the proposed technique relied on single-shot 2D acquisitions, that are prone to blurring in the slice direction due to thickened slices as a result of imperfect slice profiles.

In conclusion, the developed single-shot SMS DENSE method is capable of consistently assessing the brain tissue strain tensor on a voxel-wise level, despite the amplified noise introduced by the use of spatial derivatives. Through a principle component analysis, we successfully derived the principal strain directions, and illustrated the Poisson effect in vivo in brain tissue. Besides, we derived the volumetric strain and octahedral shear strain. Volumetric strain measurements were consistent with physiological blood volume change and CSF flow through the spinal canal. Shear strain can be interpreted as a metric of inequality of the three principal strains, indicating to what extent an induced volumetric strain is achieved by equal expansion of the tissue element in all directions. This novel method provides a tool to visualize and study tissue dynamics that reflect fundamental aspects of both the microvascular function as well as mechanical properties of tissue and holds potential to serve for detecting abnormalities in tissue deformation in disease.

Credit author statement

Jacob-Jan Sloots: Conceptualization, Methodology, Software, Visualization, Data curation, Formal analysis, Writing- Original draft preparation. **Geert Jan Biessels:** Supervision, Funding acquisition, Writing – review & editing. **Alberto de Luca:** Software, Visualization, Writing – review & editing. **Jaco Zwanenburg:** Supervision, Conceptualization, Methodology, Funding acquisition, Writing – review & editing

Data availability

The data that support the findings of this study are available from the corresponding author upon request.

Code availability

The custom MATLAB software that was used for offline analysis of the data is available from the corresponding author upon request.

Acknowledgments

The research leading to these results was supported by Vici Grant 918.16.616 from the Netherlands Organization for Scientific Research (NWO) awarded to Geert Jan Biessels and the European Union's Horizon 2020 research and innovation program under grant agreement no. 666881, SVDs@target.

Supplementary materials

Supplementary material associated with this article can be found, in the online version, at doi:10.1016/j.neuroimage.2021.118078.

References

Adams, A.L., Kuijf, H.J., Viergever, M.A., Luijten, P.R., Zwanenburg, J.J.M, 2019. Quantifying cardiac-induced brain tissue expansion using DENSE. NMR Biomed 32, e4050.
Adams, A.L., Viergever, M.A., Luijten, P.R., Zwanenburg, J.J.M, 2020. Validating faster DENSE measurements of cardiac-induced brain tissue expansion as a potential tool for investigating cerebral microvascular pulsations. Neuroimage 208, 116466.
Ahn, S., Lee, S.K., 2011. Diffusion tensor imaging: exploring the motor networks and clinical applications. Korean J. Radiol. 12, 251–261.
Aletras, A.H., Ding, S., Balaban, R.S., Wen, H., 1999. DENSE: displacement Encoding with stimulated echoes in cardiac functional MRI. J. Magn. Reson. 137, 247–252.
Alperin, N., Lee, S.H., Sivaramakrishnan, A., Hushek, S.G., 2005. Quantifying the effect of posture on intracranial physiology in humans by MRI flow studies. J. Magn. Reson. Imaging 22, 591–596.
Andersson, J.L.R., Skare, S., Ashburner, J, 2003. How to correct susceptibility distortions in spin-echo echo-planar images: application to diffusion tensor imaging. Neuroimage 20, 870–888.
Artzi, M., et al., 2015. Human cerebral blood volume measurements using dynamic contrast enhancement in comparison to dynamic susceptibility contrast MRI. Neuroradiology 57, 671–678.
Asgari, M., De Zélicourt, D., Kurtcuoglu, V., 2016. Glymphatic solute transport does not require bulk flow. Sci. Rep. 6, 38635.
Bakker, E.N.T.P.T.P, et al., 2016. Lymphatic clearance of the brain: perivascular, Paravascular and significance for neurodegenerative diseases. Cell. Mol. Neurobiol. 36, 181–194.
Balédent, O., et al., 2004. Relationship between cerebrospinal fluid and blood dynamics in healthy volunteers and patients with communicating hydrocephalus. Invest. Radiol. 39, 45–55.
Balédent, O., 2012. In: Imaging of the Cerebrospinal Fluid Circulation, 9781107031777. Cambridge University Press, pp. 121–138 Cambridge University Press.
Barth, M., Breuer, F., Koopmans, P.J., Norris, D.G., Poser, B.A., 2016. Simultaneous multislice (SMS) imaging techniques. Magn. Reson. Med. 75, 63–81.
Basser, P.J., Mattiello, J., LeBihan, D., 1994. MR diffusion tensor spectroscopy and imaging. Biophys. J. 66, 259–267.
Bulte, D., Chiarelli, P., Wise, R., Jezzard, P., 2007. Measurement of cerebral blood volume in humans using hyperoxic MRI contrast. J. Magn. Reson. Imaging 26, 894–899.
Chistiakov, D.A., Orekhov, A.N., Bobryshev, Y.V., 2017. Effects of shear stress on endothelial cells: go with the flow. Acta Physiologica 219, 382–408.
Dai, G., et al., 2004. Distinct endothelial phenotypes evoked by arterial waveforms derived from atherosclerosis-prone and atherosclerosis-protected regions of the human vasculature. Cardiovasc. Pathol. 13, 26.
Davies, P.F., Civelek, M., Fang, Y., Fleming, I., 2013. The atherosusceptible endothelium: endothelial phenotypes in complex haemodynamic shear stress regions in vivo. Cardiovasc. Res. 99, 315–327.
De Guio, F., et al., 2014. Loss of venous integrity in cerebral small vessel disease: a 7-T MRI study in cerebral autosomal-dominant arteriopathy with subcortical infarcts and leukoencephalopathy (CADASIL). Stroke 45, 2124–2126.
De Leeuw, H., Bakker, C.J.G, 2012. Correction of gradient echo images for first and second order macroscopic signal dephasing using phase derivative mapping. Neuroimage 60, 818–829.
DE Simone, R., Ranieri, A., Bonavita, V., 2017. Starling resistors, autoregulation of cerebral perfusion and the pathogenesis of idiopathic intracranial hypertension. Panminerva Med 59, 76–89.
Feinberg, D.A., Mark, A.S., 1987. Human brain motion and cerebrospinal fluid circulation demonstrated with MR velocity imaging. Radiology 163, 793–799.
Fonov, V., Evans, A., McKinstry, R., Almli, C., Collins, D., 2009. Unbiased nonlinear average age-appropriate brain templates from birth to adulthood. Neuroimage 47, S102.
Fonov, V., et al., 2011. Unbiased average age-appropriate atlases for pediatric studies. Neuroimage 54, 313–327.
Frahm, J., Merboldt, K.D., Hänicke, W., Haase, A., 1985. Stimulated echo imaging. J. Magn. Reson. 64, 81–93.
Fung, Y.C., 1994. Yuan-cheng). A first Course in Continuum mechanics : For Physical and Biological Engineers and Scientists. Prentice Hall.

Greitz, D., et al., 1992. Pulsatile brain movement and associated hydrodynamics studied by magnetic resonance phase imaging. Neuroradiology 34, 370–380.
Hahn, M., Klyscz, T., Jünger, M., 1996. Synchronous measurements of blood pressure and red blood cell velocity in capillaries of human skin. J. Invest. Dermatol. 106, 1256–1259.
Hetzer, S., et al., 2018. Perfusion alters stiffness of deep gray matter. J. Cereb. Blood Flow Metab. 38, 116–125.
Hirsch, S., et al., 2013. In vivo measurement of volumetric strain in the human brain induced by arterial pulsation and harmonic waves. Magn. Reson. Med. 70, 671–682.
Holdsworth, S.J., Rahimi, M.S., Ni, W.W., Zaharchuk, G., Moseley, M.E., 2016. Amplified magnetic resonance imaging (aMRI). Magn. Reson. Med. 75, 2245–2254.
Jezzard, P., Balaban, R.S., 1995. Correction for geometric distortion in echo planar images from B0 field variations. Magn. Reson. Med. 34, 65–73.
Jin, X., Zhu, F., Mao, H., Shen, M., Yang, K.H., 2013. A comprehensive experimental study on material properties of human brain tissue. J. Biomech. 46, 2795–2801.
Klein, S., Staring, M., Murphy, K., Viergever, M.A., Pluim, J.P.W.Elastix:, 2010. A toolbox for intensity-based medical image registration. IEEE Trans. Med. Imaging doi:10.1109/TMI.2009.2035616.
Kuijf, H.J., et al., 2016. Quantification of deep medullary veins at 7 T brain MRI. Eur. Radiol. 26, 3412–3418.
Leemans, A., Jones, D.K., 2009. The B-matrix must be rotated when correcting for subject motion in DTI data. Magn. Reson. Med. 61, 1336–1349.
Linninger, A.A., et al., 2005. Pulsatile cerebrospinal fluid dynamics in the human brain. IEEE Trans. Biomed. Eng. 52, 557–565.
Linninger, A.A., et al., 2009. A mathematical model of blood, cerebrospinal fluid and brain dynamics. J. Math. Biol. 59, 729–759.
McGarry, M.D.J.J, et al., 2011. An octahedral shear strain-based measure of SNR for 3D MR elastography. Phys. Med. Biol. 56, N153–N164.
Mestre, H., Kostrikov, S., Mehta, R.I., Nedergaard, M., 2017. Perivascular spaces, glymphatic dysfunction, and small vessel disease. Clin. Sci. 131, 2257–2274.
Mori, S., Crain, B.J., Chacko, V.P., Zijl, P.C.M.Van, 1999. Three-dimensional tracking of axonal projections in the brain by magnetic resonance imaging. Ann. Neurol. 45, 265–269.
Mucke, J., et al., 2015. Asymmetry of deep medullary veins on susceptibility weighted MRI in patients with acute MCA stroke is associated with poor outcome. PLoS One 10.
Pahlavian, S.H., Oshinski, J., Zhong, X., Loth, F., Amini, R., 2018. Regional quantification of brain tissue strain using displacement-encoding with stimulated echoes magnetic resonance imaging. J. Biomech. Eng. 140, 081010.
Pajevic, S., Pierpaoli, C., 1999. Color schemes to represent the orientation of anisotropic tissues from diffusion tensor data: application to white matter fiber tract mapping in the human brain. Magn. Reson. Med. 42, 526–540.
Pantoni, L., 2010. Cerebral small vessel disease: from pathogenesis and clinical characteristics to therapeutic challenges. Lancet Neurol 9, 689–701.
Reese, T.G., Feinberg, D.A., Dou, J., Wedeen, V.J., 2002. Phase contrast MRI of myocardial 3D strain by encoding contiguous slices in a single shot. Magn. Reson. Med. 47, 665–676.
Sack, I., et al., 2009. The impact of aging and gender on brain viscoelasticity. Neuroimage 46, 652–657.
Sack, I., Streitberger, K.-J.J., Krefting, D., Paul, F., Braun, J., 2011. The influence of physiological aging and atrophy on brain viscoelastic properties in humans. PLoS One 6, e23451.
Shore, A.C., Sandeman, D.D., Tooke, J.E., 1995. Capillary pressure, pulse pressure amplitude, and pressure waveform in healthy volunteers. Am. J. Physiol. - Hear. Circ. Physiol. 268.
Sloots, J.J., Luijten, P.R., Biessels, G.J., Zwanenburg, J.J.M, 2019. Optimizing the DENSE Sequence for Accurate Brain Tissue Strain Measurements at 7T MRI. ISMRM Proc 2800.
Sloots, J.J., Luijten, P.R., Biessels, G.J., Zwanenburg, J.J.M, 2019. Cardiac and respiratory induced 3d brain tissue strain as marker of physiological blood volume dynamics at 7T MRI. ISMRM Proc 2799.
Sloots, J.J., Biessels, G.J., Zwanenburg, J.J.M, 2020. Cardiac and respiration-induced brain deformations in humans quantified with high-field MRI. Neuroimage 210.
Soellinger, M., Rutz, A.K., Kozerke, S., Boesiger, P., 2009. 3D cine displacement-encoded MRI of pulsatile brain motion. Magn. Reson. Med. 61, 153–162.
Spector, R., Robert Snodgrass, S., Johanson, C.E., 2015. A balanced view of the cerebrospinal fluid composition and functions: focus on adult humans. Exp. Neurol. 273, 57–68.
Spottiswoode, B.S., et al., 2007. Tracking myocardial motion from cine DENSE images using spatiotemporal phase unwrapping and temporal fitting. IEEE Trans. Med. Imaging 26, 15–30.
Ståhlberg, F., et al., 1989. A method for MR quantification of flow velocities in blood and CSF using interleaved gradient-echo pulse sequences. Magn. Reson. Imaging 7, 655–667.
Tan, L., et al., 2017. A numerical framework for interstitial fluid pressure imaging in poroelastic MRE. PLoS One 12, e0178521.
Terem, I., et al., 2018. Revealing sub-voxel motions of brain tissue using phase-based amplified MRI (aMRI). Magn. Reson. Med. 80, 2549–2559.
Vonken, E.J.P.A., Van Osch, M.J.P., Bakker, C.J.G., Viergever, M.A, 1999. Measurement of cerebral perfusion with dual-echo multi-slice quantitative dynamic susceptibility contrast MRI. J. Magn. Reson. Imaging 10, 109–117.
Wåhlin, A., et al., 2012. Phase contrast MRI Quantification of pulsatile volumes of brain arteries, veins, and cerebrospinal fluids compartments: repeatability and physiological interactions. J. Magn. Reson. Imaging 35, 1055–1062.
Wardlaw, J.M., Smith, C., Dichgans, M., 2013. Mechanisms of sporadic cerebral small vessel disease: insights from neuroimaging. Lancet Neurol 12, 483–497.
Weaver, J.B., et al., 2012. Brain mechanical property measurement using MRE with intrinsic activation. Phys. Med. Biol. 57, 7275–7287.
Yan, S., et al., 2014. Increased Visibility of Deep Medullary Veins in Leukoaraiosis: a 3-T MRI Study. Front. Aging Neurosci. 6, 144.
Zhong, X., et al., 2009. Tracking brain motion during the cardiac cycle using spiral cine–DENSE MRI. Med. Phys. 36, 3413–3419.
Zorgani, A., et al., 2015. Brain palpation from physiological vibrations using MRI. Proc. Natl. Acad. Sci. U. S. A. 112, 12917–12921.